

Do anomalously-dense hot Jupiters orbit stealth binary stars?

Tanvi Goswamy¹, Andrew Collier Cameron^{1*}, Thomas G. Wilson¹

¹*Centre for Exoplanet Science, SUPA School of Physics and Astronomy, University of St Andrews, St Andrews, Fife KY16 9SS, UK*

Accepted 2024 September 02. Received 2024 August 26; in original form 2024 July 03

ABSTRACT

The Wide Angle Search for Planets (WASP) survey used transit photometry to discover nearly 200 gas-giant exoplanets and derive their planetary and stellar parameters. Reliable determination of the planetary density depends on accurate measurement of the planet’s radius, obtained from the transit depth and photodynamical determination of the stellar radius. The stellar density, and hence the stellar radius are typically determined in a model-independent way from the star’s reflex orbital acceleration and the transit profile. Additional flux coming from the system due to a bright, undetected stellar binary companion can, however, potentially dilute the transit curve and radial velocity signal, leading to under-estimation of the planet’s mass and radius, and to overestimation of the planet’s density. In this study, we cross-check the published radii of all the WASP planet host stars, determined from their transit profiles and radial-velocity curves, against radiometric measurements of stellar radii derived from their angular diameters (via the Infrared Flux method) and trigonometric parallaxes. We identify eight systems showing radiometric stellar radii significantly greater than their published photodynamical values: WASPs 20, 85, 86, 103, 105, 129, 144 and 171. We investigate these systems in more detail to establish plausible ranges of angular and radial-velocity separations within which such “stealth binaries” could evade detection, and deduce their likely orbital periods, mass ratios, and flux ratios. After accounting for the dilution of transit depth and radial velocity amplitude, we find that on average, the planetary densities for the identified stealth binary systems should be reduced by a factor of 1.3.

Key words: stars: planetary systems – stars: binaries: general – planets and satellites: fundamental parameters planets – planets and satellites: gaseous planets – techniques: photometric – techniques: spectroscopic

1 INTRODUCTION

The Wide-Angle Search for Planets (WASP) project (Pollacco et al. 2006) has published the discoveries of over 178 transiting gas-giant exoplanets in close orbits about their host stars (Southworth 2011).

The validation and characterisation of a WASP planet candidate involves photodynamical analysis of the transit light curve to establish the planet/star radius ratio and the stellar density from the transit depth and duration respectively (Southworth 2010). Since most WASP host stars have masses close to solar, the inverse cube root of the stellar density (in solar units) provides an approximate estimate of the stellar radius. Follow-up spectroscopy yields the stellar effective temperature, surface gravity and metallicity. This spectroscopic characterisation allows the stellar mass to be estimated. Radial-velocity observations of the host star’s orbit then determine the planetary mass.

Since the release of the *Gaia* DR2 and DR3 catalogues (Gaia Collaboration et al. 2021, 2023), the availability of precise parallaxes has made it possible to determine WASP host-star radii independently. The stellar angular diameter can be estimated from the effective temperature and an estimate of the bolometric flux received at Earth, via the Infrared Flux method (“IRFM”) of Blackwell & Shallis (1977). The angular diameter and *Gaia* parallax together yield a direct geometrical estimate of the the stellar radius. The radii determined via

this method can be compared directly with the radii inferred from photodynamical fits to their planets’ transit profiles.

The stellar radius estimates obtained via these two methods should agree unless the light of the host star is diluted significantly by a stellar binary companion. In such cases, the additional flux dilutes both the transit depth and the radial velocity amplitude. This in turn leads to an overestimation of the planet’s density and an underestimation of its radius and mass. Stellar binaries are usually detectable if the orbit is small enough that the Doppler-shifted spectral lines of the two stars are resolvable; or wide enough for the binary to be resolved through direct imaging. We coin the term “stealth binaries” to characterise systems whose orbital separations lie in the range in which they cannot be resolved by either method.

Ciardi et al. (2015) have carried out a similar study, discussing the effects of undetected multiplicity on planetary radii for Kepler Objects of Interest (KOIs). For each KOI, they found the best-fit Dartmouth isochrone, and considered all stars along the isochrones that had absolute Kepler magnitudes fainter than the primaries as viable companions. Their derivation of the theoretical correction factor X_R - by which the planetary radius would have been underestimated - is similar to the equations derived in Sections 4.3 and 4.4 of this paper. They derived mean values of X_R for all possible scenarios up to a multiplicity of 3. Payne et al. (2018) developed this concept further, using the relationship between the mean stellar density and stellar effective temperature to identify which of the stellar components in eight marginally-resolved multi-star systems were the hosts of transiting planets discovered with Kepler/K2.

* acc4@st-andrews.ac.uk

In this paper we compare the stellar radii obtained from the spectral-energy distributions and *Gaia* parallaxes of a large sample of WASP planet-host stars, against those calculated from transit fitting and spectroscopic characterisation. In the majority of cases the host stars are not known a priori to be binaries. However, if previously-undetected binaries are present in the WASP catalogue, the photodynamical host-star radii derived from the stellar density via the transit duration will be smaller than those determined from the stellar angular diameter and parallax. In cases where the discrepancy is significant, their planets' bulk densities will have been over-estimated.

Our methods are discussed in detail in Section 2. In Section 3, we present the comparison of results from both methods. In Section 4.1, we examine these systems in more detail to predict the limits on angular separation and the limiting difference in radial velocities of the two stars that would allow the secondary star to remain undetected. These limits can be used to classify these systems as "stealth binaries" and estimate the plausible range of orbital periods of the stellar binaries. Section 4.2 discusses WASP-85AB – a known stellar binary which we use to verify some of our methods. In Section 4.3, we estimate the most probable flux ratio and mass ratio for each stealth binary system. The factor by which the radii from both methods differs gives us information about how much additional flux is being received from the system – and thus an estimate on the luminosity ratio of the two stars in the binary. We then use the evolutionary tracks and isochrone tables of [Bressan et al. \(2012\)](#) to estimate the binary mass ratios from the luminosity ratios. Finally, in Section 4.4, we assess the effect of contamination of observations on the derived system parameters, and hence recalculate them after having accounted for the secondary star. Corrections to parameters for some WASP planets based on similar studies have previously been made by [Evans et al. \(2016\)](#), [Southworth et al. \(2020\)](#), and [Delrez et al. \(2018\)](#); which will be discussed in Section 4.5. We conclude the study and suggest follow-up observations in Section 5.

2 METHODS

We start by comparing the published radii of a sample of 178 host stars from the WASP survey, obtained by photodynamical modelling of their transit profiles, with radii estimated from their angular diameters and parallaxes.

Photodynamical modelling of planetary transits is carried out routinely as part of the discovery process leading to the announcement of a new planet. [Winn \(2009\)](#) reviewed the planetary and stellar parameters that can be measured from precise photometry of exoplanet transits combined with radial-velocity follow-up. The transit duration (T) gives us an estimate of the stellar density as per Eq. 1 for central transits, and the transit depth (δ) gives us the ratio of the planetary radius (R_p) to the stellar radius (R_s), as per the relation $\sqrt{\delta} = R_p/R_s$.

$$\frac{T}{3 \text{ h}} \approx \left(\frac{P}{4 \text{ days}} \right)^{1/3} * \left(\frac{\rho_s}{\rho_\odot} \right)^{-1/3} \quad (1)$$

Here, P is the orbital period of the planet, and ρ_s is the stellar density. Since most FGK main sequence stars have a mass close to unity, their radius R_s can be estimated directly from the density. Dilution of the transit curve due to flux from a potential binary companion will not cause a change in the transit duration – which is why we can rely on the R_s calculation from this method (hereon " R_{trans} ") to compare results from the IRFM. However, it will cause a decrease in δ and thus an underestimation of R_p .

R_s can also be derived from the spectrum of the star using the IRFM, which gives us the star's effective temperature (T_{eff}). This method was first proposed by [Blackwell & Shallis \(1977\)](#), after which various improved scales have been proposed. The basic idea of the IRFM is to compare the ratio between the bolometric flux (f_{bol}) and the flux in a given IR bandpass (f_{IR}) – both received at the Earth's atmosphere; to the ratio between the stellar surface bolometric flux (σT_{eff}^4) and the surface flux in the same IR bandpass ($F_{\text{IR, model}}$), which is determined theoretically using the stellar T_{eff} , stellar surface gravity $\log g$, and [Fe/H] values from the star's spectrum ([Casagrande et al. 2010](#)). This is shown in Eq. 2, where T_{eff} is the only unknown quantity:

$$\frac{f_{\text{bol}}}{f_{\text{IR}}} = \frac{\sigma T_{\text{eff}}^4}{F_{\text{IR, model}}} \quad (2)$$

Using T_{eff} along with the f_{bol} received from the star and the parallax from *Gaia* DR3 ([Gaia Collaboration et al. 2023](#)) extracted using *VizieR*¹ ([Ochsenbein, Bauer, & Marcout 2000](#)), R_s (hereon " R_{IRFM} ") can be calculated using Eq. 3:

$$f_{\text{bol}} = \sigma T_{\text{eff}}^4 \left(\frac{R_s}{d} \right)^2 \quad (3)$$

Here, d is the distance to the star given by the inverse of the parallax, and σ is the Stefan-Boltzmann constant.

In this study we estimate the angular diameter by fitting the apparent magnitudes in eight optical/IR bandpasses: *Gaia* BP, G and RP ([Gaia Collaboration et al. 2023](#)); 2MASS J, H and Ks ([Skrutskie et al. 2006](#)); and WISE W1 and W2 ([Wright et al. 2010](#)), with synthetic photometry derived from the stellar model atmospheres of [Castelli & Kurucz \(2003\)](#). While other bandpasses can be used in addition to these, this set has two advantages: they are available for all the WASP host stars, and the angular-diameter values derived from them are independent of degeneracies between stellar effective temperature and interstellar reddening ([Schanche et al. 2020](#)). At the distances of typical WASP host stars, the parallax and the angular diameter combine to yield the stellar radius to a precision of order 1 to 2 percent. This is comparable to the precision achievable with asteroseismology (e.g. [Silva Aguirre et al. 2015, 2017](#)).

Our aim is to compare the values of R_s using both the methods above for all the WASP systems. The stars that have a larger R_s from the IRFM than from photodynamical modelling (i.e., $R_{\text{IRFM}} > R_{\text{trans}}$) are our targets of interest.

3 RESULTS

We have used *TEPCat*² ([Southworth 2011](#)) to extract all our data on the WASP systems. Because the discovery papers for the majority of these planets were published prior to the *Gaia* DR2 and DR3 data releases, the published R_s values have in most cases been obtained using the transit duration method. We performed the IRFM calculations using Python routines³ developed by the authors, based on the *ASTROQUERY* ([Ginsburg et al. 2021](#)), *PYSYNPHOT* ([STScI Development Team 2013](#)) and *PYPHOT* ([Fouesneau 2022](#)) packages, on all the systems to check the consistency with the published values. The inferred stellar radii are plotted against the values catalogued

¹ <https://vizier.cds.unistra.fr/viz-bin/VizieR-3?-source=I/355/gaiadr3>

² <https://www.astro.keele.ac.uk/jkt/tepcat/allplanets-noerr.html>

³ Routines used are in the file "GaiaIRFM_EDR3.py"

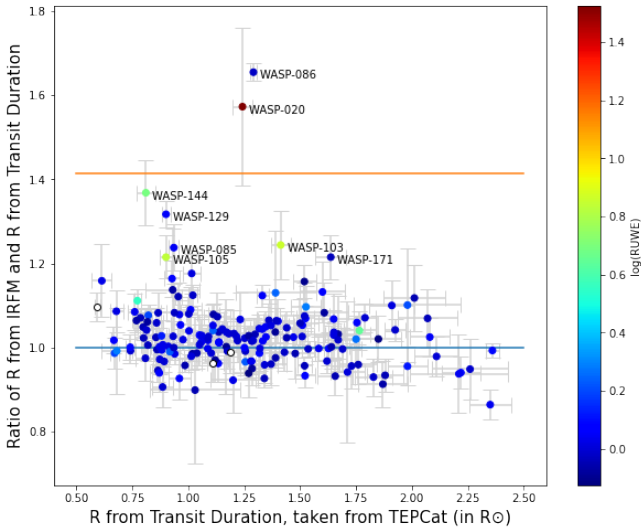


Figure 1. Ratio of radii from IRFM (R_{IRFM}) and published photodynamical values taken from TEPcat (R_{trans}) vs R_{trans} , along with error bars. Most of the points lie along the equality line (light blue), while some of the stars (labelled in the graph) lie closer to, or even above, the $\sqrt{2}$ line (orange). The points are colour-coded based on their RUWE values taken from Gaia DR3, while the stars missing from the catalogue are in white.

in TEPcat, in Fig. 1. We have also extracted the renormalised unit weight error (RUWE) values for each star from Gaia DR3, which should be ≈ 1 for single sources (Gaia Collaboration et al. 2023). The RUWE is similar in character to the reduced χ^2 statistic; Ziegler et al. (2020) note that values in excess of 1.4 are indicative of an extended or binary source in Gaia DR2, while Penoyre, Belokurov, & Evans (2022) and Castro-Ginard et al. (2024) suggest a lower threshold of order 1.25 for Gaia DR3. The points on the graph in Fig. 1 are colour-coded by their RUWE values to highlight outliers with high RUWE.

The radiometric stellar radii were derived from the angular diameter (obtained from the apparent bolometric flux and effective temperature derived from the synthetic photometry via eqs. 2 and 3) and the Gaia parallax. These were then compared with the photodynamical stellar radii R_{trans} obtained from TEPcat, which in the source publications had generally been computed under the assumption that no contaminating light was present.

We have identified 8 clear outliers in Fig. 1 which lie significantly above the $R_{\text{trans}} = R_{\text{IRFM}}$ line, but near or below the $R_{\text{IRFM}} = \sqrt{2}R_{\text{trans}}$ line along which binaries with equal-luminosity components should lie. Six of these eight WASP hosts (WASP-85, 103, 105, 129, 144, 171) have $R_{\text{trans}} < R_{\text{IRFM}} \lesssim \sqrt{2}R_{\text{trans}}$, while WASPs 20 and 86 lie above the line. Half of these also have high RUWE values, as indicated by their colours on the graph, which provides further evidence of binarity (Belokurov et al. 2020). We note that WASP-86 (Faedi et al. 2016), has recently been identified as the same star as KELT-12 (Stevens et al. 2017). The apparent discrepancy in the stellar radii reported in these two discovery papers has recently been reconciled by Southworth & Faedi (2022). This star has a long and shallow transit, causing the initial discrepancy in measurement of its properties in the two discovery papers. We will hence not include WASP-86 in our analysis. The revised radius can be found in Southworth & Faedi (2022). Out of the remaining seven stars, WASP-20 and WASP-85 are known binary systems. We will look at WASP-85 in more detail in a later section as we have

sufficient information about its binary companion from the discovery paper itself. WASP-20 will be discussed in Section 4.5.

4 DISCUSSION

Since we have identified the systems where we suspect the presence of a bright, unresolved secondary star diluting the transit curve, we can now begin our investigation of these systems in more detail. The next few sections discuss the various studies that we carried out on these 7 systems.

We first investigate the reasons why the companion star has not been detected yet.

4.1 Radial velocity difference and angular separation

The transit depth can be diluted due to background stars that may not be bound to the primary star. It is unlikely, however, that such a chance alignment would involve two physically unrelated stars with indistinguishable radial velocities. The absence of two resolvable spectra therefore allows us to assume that the two stars form a wide but bound pair, and that the dilution is caused by a secondary star that has a RV very close to that of the primary. For the two stars' spectra to be unresolved with a radial-velocity spectrometer such as SOPHIE, CORALIE or HARPS, the Doppler shift between the two stars' spectral lines would have to be close enough for their cross-correlation function to have a single peak. To estimate the detection threshold for such a binary, we approximated the CCFs of slowly-rotating solar-type stars as Gaussian profiles with the same width as the CCF of the Sun observed with the HARPS-N solar telescope feed (Collier Cameron et al. 2019), as shown in Fig. 2.

For RV separations less than $\Delta RV = 8$ km/s, the combined signal appears like that of a single star, with no sign of the presence of a companion. Above that, the combined signal broadens and develops significant kurtosis, before separating into a recognisably bimodal profile. We therefore set our upper limit on for stealth binaries at $\Delta RV < 8$ km s $^{-1}$.

It is also possible for stealth binaries to be mistaken for planet-host systems in the absence of high-resolution spectra, as discussed by Marcussen & Albrecht (2023). They found that the primary false-positive scenario for astrometric exoplanet detections is an unresolved binary system with alike components and a small photocentric orbit.

Another factor that can allow a contaminating secondary star to evade detection during the RV follow-up is the angular separation (θ) between the two stars. If θ is less than the fibre diameter of the instrument used, then the measured RV of the primary star will be contaminated. Spectroscopic follow-up for the WASP systems is usually done using the SOPHIE (Perruchot et al. 2008) or CORALIE (Baranne et al. 1996; Queloz et al. 2000), instruments. These have fibre-aperture diameters of 3" and 2" respectively – which means any binaries with θ significantly less than the fibre diameter would not be detectable. However, the aperture size of the HARPS (Mayor et al. 2003) spectrograph is 1" and this instrument was used for follow-up on WASP-85, which is why we set our lower limit for detection at $\theta = 1$ ".

Given the masses of the two stars and an estimate of the orbital period, the physical separation a between the two stars follows from Kepler's 3rd law. Together with the parallax ($\hat{\pi}$) from Gaia, this yields the angular separation. In solar units,

$$\frac{\theta}{1 \text{ arcsec}} = \left(\frac{\hat{\pi}}{1 \text{ arcsec}} \right) \left(\frac{P}{1 \text{ y}} \right)^{2/3} \left(\frac{M_1 + M_2}{M_\odot} \right)^{1/3}. \quad (4)$$

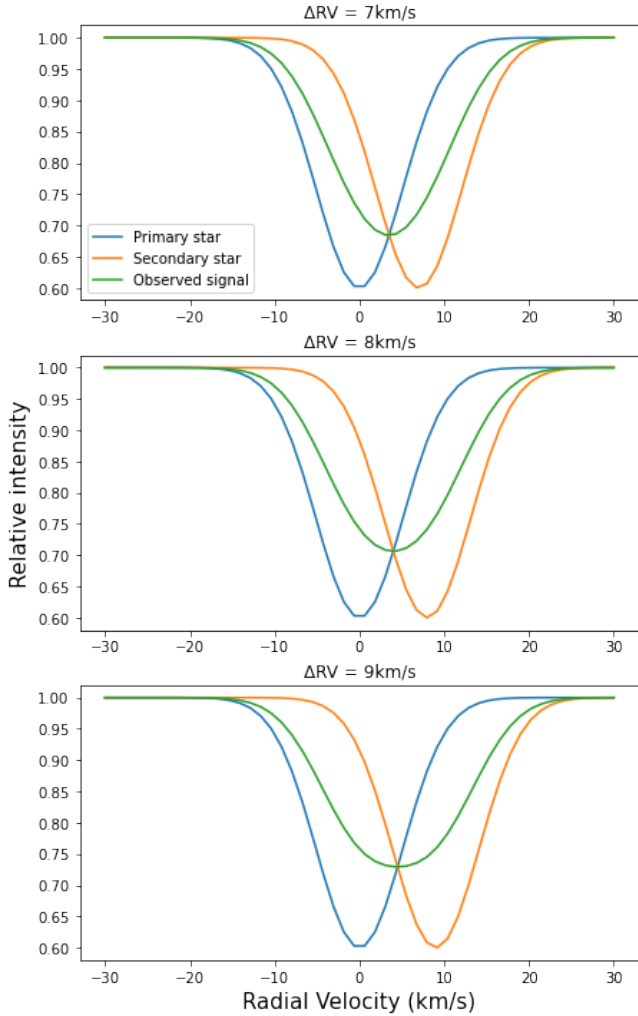


Figure 2. Synthetic cross-correlation functions of model binaries, comprising pairs of gaussian profiles with radial-velocity separations of 7, 8 and 9 km s⁻¹. A single broad peak is seen at separations up to 9 km s⁻¹. At greater separations, the composite profile becomes bimodal, and the binary nature becomes evident.

The maximum radial-velocity separation ΔRV , assuming a circular orbit viewed edge-on, follows from energy conservation and Kepler’s 3rd law:

$$\frac{\Delta RV}{v_{\oplus}} = \left(\frac{M_1 + M_2}{M_{\odot}} \right)^{1/2} \left(\frac{a}{1 \text{ au}} \right)^{-1/2} = \left(\frac{M_1 + M_2}{M_{\odot}} \right)^{1/3} \left(\frac{P}{1 \text{ y}} \right)^{-1/3}, \quad (5)$$

scaling to the Earth’s orbital velocity $v_{\oplus} \approx 30 \text{ km s}^{-1}$.

In Fig. 3 we plot the ΔRV values obtained using Eq. 5 as a function of the angular separation θ computed with Eq. 4 for each of the seven WASP host stars with anomalous radii, on a logarithmic grid of periods spanning the range 1–10⁵ years. The total mass is assumed to be between 1.5 and 2 times that of the planet-hosting star. Planets are preferentially identified around the brighter components of binaries when the observations are signal-to-noise-limited. The mass ratio distribution of binary systems is quite flat, so a reasonable assumption might be that the total mass is on average ~ 1.5 times that of the planet-host star if its stellar companion is bright enough to affect the overall angular diameter. If we also make allowance for cases where

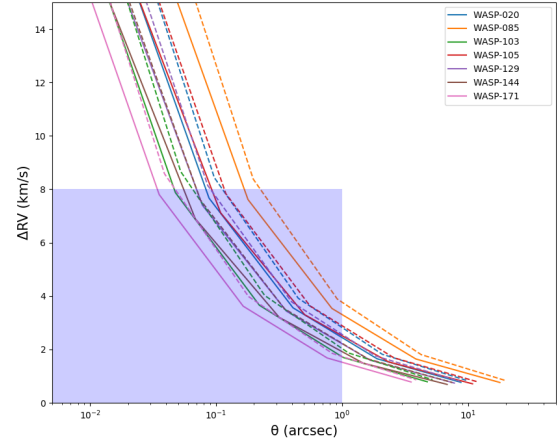


Figure 3. Radial velocity difference (ΔRV in km/s) vs angular separation (θ) in arcsec. Each curve corresponds to the marked WASP-planet host, and each point on a curve corresponds to a particular value for orbital period. The portion of each curve that lies within the blue box corresponds to the parameters that the system should have in order to escape detection as a “stealth binary”. Solid lines denote a model assuming that the total mass of the binary system is 1.5 times the primary mass. Dashed lines show the effect of assuming the total mass to be twice that of the primary.

Table 1. Minimum and maximum orbital periods and angular separations ($\theta_{\text{max}} = 1''$) corresponding to the stealth binaries box assuming a system mass 1.5 times the primary mass.

WASP host star	P_{max} (yrs)	P_{min} (yrs)	θ_{min} (arcsec)
WASP-020	3837	88	0.08
WASP-085	1319	86	0.16
WASP-103	9651	95	0.05
WASP-105	2792	70	0.09
WASP-129	4600	79	0.07
WASP-144	5600	64	0.05
WASP-171	15049	93	0.03

the luminosity ratio is close to 1 and the planet orbits the fainter star, an assumed mass ratio closer to 2 might be preferable. Figure 3 shows that the difference between these two assumptions has little practical impact on the inferred angular and radial-velocity separations.

The blue box indicates the limits on ΔRV and θ below which we anticipate the binary to remain undetected; i.e., to lie within the hiding zone. Each point on the curve for any WASP host corresponds to a particular estimate on the period of the two stars. Thus, using the boundaries of our “stealth binaries box”, we calculate the minimum and maximum period, as well as the minimum possible angular separation. These are summarised in Table 1. Increasing the assumed system mass to twice that of the primary decreases the maximum period by about 15 percent and increases the minimum period by 30 percent. The minimum angular separation increases by about 35 percent.

The periods obtained are in the range of a hundred to a few thousand years. This explains naturally why none of these systems could have been detected as a spectroscopic binary in the decade or so since their discovery.

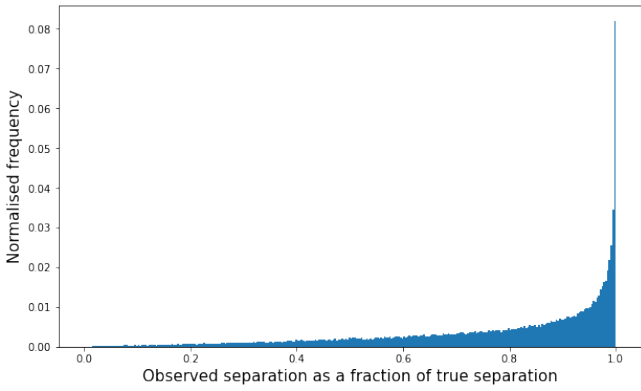


Figure 4. Probability distribution of the ratio of observed angular separation to the true angular separation. For an angle θ between the line connecting the two stars and the line of sight to the observer, $\sin \theta$ gives us this ratio. The curve has been obtained by sampling from a uniform distribution in $\cos \theta$ between -1 and 1 to calculate the corresponding values of $\sin \theta$ (cf. Collier Cameron 2016; Hatzes 2016).

4.2 WASP-85

The binary companion of WASP-85A was detected during its discovery by Brown et al. (2014). From the discovery paper, we took the values for the mass of the companion, and the observed angular separation from *Gaia* DR3 to get the corresponding orbital period from Eq. 4. To estimate the true orbital separation from the observed angular separation, we must take into account the random orbit orientation. The distribution of apparent angular separation as a fraction of true separation depends on the angle between the line connecting the stellar centres (assumed randomly oriented in space) and the line of sight. Fig. 4 shows this probability distribution, with a mean of 0.79. Thus, on average, we only observe 80% of the true angular separation.

The *Gaia* DR3 catalogue gives the observed angular separation of the WASP-85AB binary system as $\theta = 1.28''$; this suggests a true angular separation of about $1.6''$. On the plot of ΔRV vs θ in Fig. 3, this angular separation corresponds to a ΔRV of 2.78 km/s and an orbital period of 2500 years, which is in good agreement with the estimate of 2000–3000 years in the discovery paper.

The companion star (WASP-85B) is about 0.9 mag fainter in the G band than the primary star, with a flux ratio of about 0.5 in most bands. The discovery paper gives a mass $M_B = 0.88 \pm 0.07 M_\odot$ and a radius $R_B = 0.77 \pm 0.13 R_\odot$. If we take the photodynamical radius of the primary $R_{A,\text{trans}} = 0.935 R_\odot$ and scale it by the square root of the flux ratio $f_{A+B}/f_A \approx 1.5$, we expect to obtain $R_{\text{IRFM}} = 1.16 R_\odot$ when the light of both components is combined.

Since *Gaia* was able to resolve the system, we combined the *Gaia* magnitudes for the primary and secondary stars to recalculate the total flux coming from the system and hence the combined *Gaia* BP, G and RP magnitudes. Combining these with the 2MASS and WISE magnitudes (in which the binary is unresolved), the resulting angular diameter and parallax yielded $R_{\text{IRFM}} = 1.16 R_\odot$. This confirms that the angular radius derived from the combined spectral energy distribution of both binary components is overestimated by an amount that is consistent with our knowledge of the two stars. This means that in cases where $R_{\text{trans}} < R_{\text{IRFM}} \lesssim \sqrt{2} R_{\text{trans}}$, there is a strong possibility that the planet orbits the brighter component of a stealth binary. There may indeed be cases where the luminosity ratio is close to 1, and a planet orbiting the fainter component produces detectable transits. In

Table 2. Some parameters of the outliers taken from TEPcat and discovery papers, used for further analysis in this section.

WASP host star	R_S (in R_\odot)	M_S (in M_\odot)	Age (Gyrs)
WASP-020	1.242	1.113	4.0
WASP-085	0.935	1.090	0.3
WASP-103	1.413	1.205	4.0
WASP-105	0.900	0.890	6.0
WASP-129	0.900	1.000	1.0
WASP-144	0.810	0.810	8.0
WASP-171	1.637	1.171	6.0

such cases, it would be possible to obtain $R_{\text{IRFM}} \gtrsim \sqrt{2} R_{\text{trans}}$. This could explain the location of the system WASP-20, above the orange line in Fig. 1, as discussed in Section 4.5.

4.3 Predicting flux and mass ratios

We now use the information we have about the companion star to make estimates on the flux and mass ratios with respect to the primary star for each of our outliers. We use isochrones from Bressan et al. (2012) to relate stellar masses to magnitudes. Table 2 shows some of the parameters of the primary stars that we have used for our analysis in this section. The stellar radii and masses have been taken from TEPcat, while the rough age estimates have been taken from the discovery papers.

Using these isochrones, we estimated the ratio of fluxes of the primary to the companion star. We evaluated the flux ratio for every mass ratio $q = M_2/M_1$ from 0.7 to 1.2 in intervals of 0.01. We also computed the most probable flux ratio from the factor r by which R_{IRFM} is greater than the actual radius; i.e., $1 + \frac{f_2}{f_1} = r^2$ where f_2 and f_1 are the fluxes received from the secondary and primary stars respectively. Each value of r corresponds to a different value of q , found by interpolating the isochrone for a star of the same age, assuming that the age of the companion is the same as that of the primary star. These results are summarised in Table 3, while Fig. 5 shows the probability curves for the factor r , given the value that was observed.

All the most-probable mass ratios are within the range 0.89–1, barring WASP-20. For this system, r has a value greater than $\sqrt{2}$, implying that $f_2 > f_1$; i.e., the secondary star is brighter than the primary, and the planet is orbiting the fainter and hence denser star. The identity of the planet-hosting component of the binary is discussed in Section 4.5.

4.4 Recalculating planetary parameters

Using the most probable flux ratios calculated in the previous section, we can obtain the value of the factor ‘ r ’ and use this to correct the planet’s radius R_p , mass M_p , and density ρ_p . We know that:

$$\sqrt{\delta} \propto R_p \text{ and } \delta \propto R^2 \Rightarrow R_p \propto r$$

where δ is the transit depth. From Collier Cameron (2016):

$$\rho_p \propto \frac{K}{(R_p)^3} \text{ and } K \propto r^2 \Rightarrow \rho_p \propto r^{-1} \text{ and } M_p \propto r^2$$

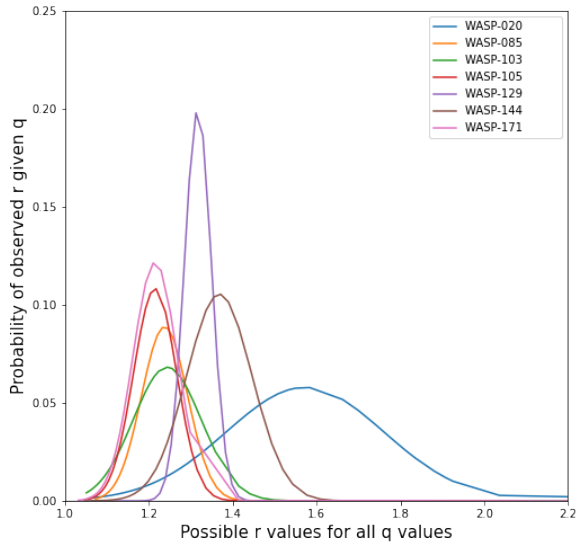
K is the RV amplitude, whose observed value is the flux-weighted average of all the K values for each star. Using the above relations and the published values of these quantities, we recalculated the planetary parameters, as summarised in Table 4.

Table 3. Most probable value for factor r , with mass ratio and flux ratio, and errors.

WASP host star	Most Probable r	Observed r	Most Probable Flux Ratio	Most Probable Mass Ratio
WASP-020	1.58 ± 0.19	1.57	1.51 ± 0.36	1.07
WASP-085	1.23 ± 0.05	1.24	0.52 ± 0.05	0.88
WASP-103	1.24 ± 0.08	1.24	0.55 ± 0.07	0.92
WASP-105	1.22 ± 0.05	1.21	0.48 ± 0.04	0.89
WASP-129	1.31 ± 0.03	1.32	0.72 ± 0.04	0.94
WASP-144	1.37 ± 0.08	1.37	0.88 ± 0.10	0.98
WASP-171	1.21 ± 0.05	1.21	0.46 ± 0.04	0.94

Table 4. Final corrected planetary parameters for all the outliers, after having accounted for the additional flux from the secondary star. The fractional error in each quantity remains the same. Original references for photodynamical values adopted from TEPcat are given as footnotes. Corrections have been made using the relations discussed in Section 4.4.

WASP host star	Photodynamical R_p (in R_J)	Corrected R_p (in R_J)	Photodynamical M_p (in M_J)	Corrected M_p (in M_J)	Photodynamical ρ_p (in ρ_J)	Corrected ρ_p (in ρ_J)
WASP-020 ^a	1.46	2.31 ± 0.29	0.31	0.78 ± 0.19	0.10	0.06 ± 0.01
WASP-085 ^b	1.01	1.25 ± 0.07	0.82	1.25 ± 0.03	0.80	0.65 ± 0.02
WASP-103 ^b	1.53	1.90 ± 0.14	1.49	2.31 ± 0.33	0.42	0.34 ± 0.05
WASP-105 ^c	0.96	1.17 ± 0.06	1.80	2.67 ± 0.27	2.00	1.64 ± 0.11
WASP-129 ^d	0.93	1.22 ± 0.05	1.00	1.72 ± 0.19	1.20	0.91 ± 0.15
WASP-144 ^e	0.85	1.17 ± 0.10	0.44	0.83 ± 0.15	0.72	0.53 ± 0.11
WASP-171 ^f	0.98	1.19 ± 0.08	1.08	1.59 ± 0.20	1.13	0.93 ± 0.17

^a Photodynamical values from [Anderson et al. \(2015\)](#)^b Photodynamical values reverse-calculated using r value from Table 3, from values (in italics) already corrected for binarity in [Brown et al. \(2014\)](#) (see Sect. 4.2)^c Photodynamical values from [Gillon et al. \(2014\)](#)^d Photodynamical values from [Anderson et al. \(2017\)](#)^e Photodynamical values from [Maxted et al. \(2016\)](#)^f Photodynamical values from [Hellier et al. \(2019\)](#)^g Photodynamical values from [Nielsen et al. \(2019\)](#)**Figure 5.** Probability curves for the possible values of the factor r defined in Section 4.3, given the value that was obtained from the R_{IRFM} calculation for each host.

The surface gravity of the planet varies directly with its mass and inversely with the square of its radius. After accounting for the stealth binarity; the mass goes up by r^2 while the radius goes up by r – which means that the planet’s surface gravity remains unchanged. This is

an interesting result, as it tells us that the planetary surface gravity is immune to stealth binaries.

4.5 WASP-20 and WASP-103

The binary companion of WASP-20A was discovered at a separation of 0.26 arcsec by [Evans et al. \(2016\)](#) using near-IR adaptive-optics imaging with the SPHERE instrument on the VLT. They inferred an increase in planetary mass M_p and radius R_p by 4σ and 1σ respectively, after having accounted for the dilution to the transit curve and radial velocity amplitude. They concluded that the planet orbits the brighter of the two stars, on the grounds that the inferred stellar density in the planet-orbits-fainter-star scenario yielded an implausibly old stellar age of 16 Gyr. The inferred separation of 61 au and system mass of order $2M_\odot$ implies a period of order 340 years, and hence a radial-velocity separation $K_A + K_B \approx 5.3 \text{ km s}^{-1}$, placing it within the blue box in Fig. 3.

[Southworth et al. \(2020\)](#) made further corrections to these parameters using updated light curves and spectroscopic data. They were unable to rule out the planet-orbits-fainter-star scenario, finding a density 1.08 times solar and an age of 3.3 Gyr. In both cases, the planet’s density is reduced relative to that obtained by assuming that the host star is single. In our own study, the balance of probability in Fig. 5 suggests that the ratio of the angular and photodynamical radii is greater than 1.4 for an assumed age of 4 Gyr. Our study thus favours the planet-orbits-fainter-star scenario.

The planetary parameters for WASP-103b were also corrected in the analysis by [Delrez et al. \(2018\)](#) for the presence of a stellar companion at a separation of 0.23 arcsec. This companion was discovered in a lucky-imaging survey by [Wöllert & Brandner \(2015\)](#). It is 3.1 magnitudes fainter than the brighter star in the i' band and 2.6 mag fainter in the z' band. We find that a discrepancy remains between R_{IRFM} and the value of R_{trans} found by [Delrez et al. \(2018\)](#) even

after this correction, so we infer that the host star may have another brighter and closer companion.

In their study of the tidal deformation and orbital decay rate of WASP-103b, Barros et al. (2022) recently found that the faint visual companion of the host star was too distant and insufficiently massive to explain the inferred positive RV acceleration $a = +0.113 \pm 0.058 \text{ m s}^{-1} \text{ day}^{-1}$, whose sign is contrary to expectations for tidal orbit decay. This suggests that the unresolved stellar companion responsible for the observed excess in the stellar angular diameter could also be the cause of the anomalous observed acceleration. Using our derived value $q = 0.92$ for the stealth companion of WASP-103, we get $M_2 = 1.11 \pm 0.10 M_\odot$, where M_2 is the mass of the companion. If we assume that the unseen companion is close to superior conjunction, the host star should be accelerating away from the observer. Using the observed acceleration and the inferred secondary mass, assuming a circular orbit and a high inclination we obtain an approximate estimate of the orbital separation:

$$d = \sqrt{\frac{GM_2}{a}} \approx 71 \pm 18 \text{ au.}$$

where d is the binary separation. At maximum elongation this would give an angular separation $\theta = 0.15 \pm 0.04$ arcsec and an orbital period $P \approx 400$ y. The maximum radial-velocity separation of the two stars would then be $K_1 + K_2 = 2\pi d/P \approx 1.1$ au/yr, or 5.2 km s^{-1} . These inferred maximum angular and radial-velocity separations lie comfortably within the blue region in Fig. 3, explaining why the inferred binary companion has thus far evaded detection.

5 CONCLUSION AND SUGGESTED WORK

Various properties of transiting exoplanets can be derived from their transit photometry and RV measurements. If these get contaminated by other stars that are bound to the host star, then the calculated parameters need to be corrected by accounting for the additional flux in the system. We find that the surface gravity of the planet is a quantity that is not affected by the dilution of the transit and RV observations. We have recalculated the masses, radii, and densities for seven WASP planets (Table 4) where we suspect that the host star has a hidden stellar companion. Our estimate of the flux ratio and orbital period for the WASP-85 binary system is consistent with that obtained in the discovery paper of Brown et al. (2014). Dilution of observations for WASP-20 and WASP-103 had been accounted for previously in literature. Our comparisons of the R_{IRFM} values with estimates of the host-star radius based on the photodynamical stellar density suggest that the planet in the WASP-20 system may orbit the fainter of the two stars, and that the stealth companion of WASP 103's host star may be responsible for the apparent secular increase in the planet's orbital period.

Overall, the densities of the planets have gone down on average by a factor of 1.3. We also made estimates on the orbital periods, mass ratios and flux ratios for all seven stealth binary systems, which have been outlined in Tables 1 and 3. The most probable flux ratios range from about 0.5 to 1, and mass ratios from 0.89 to 1 - barring WASP-20, which is an exception wherein both ratios are above 1 implying that the planetary host star is the denser and fainter of the two stellar binary components. The orbital periods range from a hundred to a few thousand years, which explains why the secondary stars have not been detected in radial-velocity observations yet. Nonetheless, the example of WASP-103 discussed above suggests that long-term RV monitoring could reveal secular accelerations in systems with companions of unequal luminosity.

These binary systems appear to have angular separations below $1''$ but are not close enough to give resolvable Doppler shifts. We also suggest that follow-up observations be made using speckle imaging, lucky imaging, or adaptive optics. Speckle imaging removes effects of turbulence in the atmosphere and provides simultaneous photometric and astrometric data at sub-arcsecond precisions (Matson, Howell, & Ciardi 2019). The 'Differential Speckle Survey Instrument' (Horch et al. 2009) has successfully detected binary companions to stars in the 'Kilodegree Extremely Little Telescope' survey (Coker et al. 2018), and can thus be used for these WASP systems as well - as was done for WASP-103 (Wöllert & Brandner 2015).

DATA AVAILABILITY

The stellar and planetary data for the WASP systems investigated in this research are available in the TEPcat database curated by Dr John Southworth at the University of Keele. All other research data underpinning this publication and the PYTHON code and notebook used to prepare all diagrams in this paper will be made available through the University of St Andrews Research Portal. The research data supporting this publication can be accessed at <https://doi.org/10.17630/1ceff0e3-c2aa-40d0-996a-0d3f8d81cf19> (Goswamy et al. 2024a). The code supporting this publication can be accessed at <https://doi.org/10.17630/72a692c8-dd85-4078-99d3-8a5551727ff9> (Goswamy et al. 2024b).

ACKNOWLEDGEMENTS

Tanvi Goswamy thanks Siddharth Rangnekar for helpful discussions and assistance with preparation of the manuscript. Andrew Collier Cameron and Thomas Wilson acknowledge support from STFC consolidated grant numbers ST/R000824/1 and ST/V000861/1, and UKSA grant number ST/R003203/1. This research has made use of NASA's Astrophysics Data System. This research has made use of the VizieR catalogue access tool, CDS, Strasbourg, France.

REFERENCES

- Anderson D. R., Collier Cameron A., Hellier C., Lendl M., Lister T. A., Maxted P. F. L., Queloz D., et al., 2015, *A&A*, 575, A61. doi:10.1051/0004-6361/201423591
- Anderson D. R., Collier Cameron A., Delrez L., Doyle A. P., Gillon M., Hellier C., Jehin E., et al., 2017, *A&A*, 604, A110. doi:10.1051/0004-6361/201730439
- Baranne A., Queloz D., Mayor M., Adrianzyk G., Knispel G., Kohler D., Lacroix D., et al., 1996, *A&AS*, 119, 373
- Barros S. C. C., Akisanmi B., Boué G., Smith A. M. S., Laskar J., Ulmer-Moll S., Lillo-Box J., et al., 2022, *A&A*, 657, A52. doi:10.1051/0004-6361/202142196
- Belokurov V., Penoyre Z., Oh S., Iorio G., Hodgkin S., Evans N. W., Everall A., et al., 2020, *MNRAS*, 496, 1922. doi:10.1093/mnras/staa1522
- Blackwell D. E., Shallis M. J., 1977, *MNRAS*, 180, 177. doi:10.1093/mnras/180.2.177
- Bressan A., Marigo P., Girardi L., Salasnich B., Dal Cero C., Rubele S., Nanni A., 2012, *MNRAS*, 427, 127. doi:10.1111/j.1365-2966.2012.21948.x
- Brown D. J. A., Anderson D. R., Doyle A. P., Maxted E. G. F. L., Smalley B., McCormac J., Almenara J. M., et al., 2014, arXiv, arXiv:1412.7761
- Casagrande L., Ramírez I., Meléndez J., Bessell M., Asplund M., 2010, *A&A*, 512, A54. doi:10.1051/0004-6361/200913204
- Castelli F., Kurucz R. L., 2003, *IAUS*, 210, A20

- Castro-Ginard A., Penoyre Z., Casey A. R., Brown A. G. A., Belokurov V., Cantat-Gaudin T., Drimmel R., et al., 2024, *A&A*, 688, A1. doi:10.1051/0004-6361/202450172
- Ciardi D. R., Beichman C. A., Horch E. P., Howell S. B., 2015, *ApJ*, 805, 16. doi:10.1088/0004-637X/805/1/16
- Coker C. T., Gaudi B. S., Pogge R. W., Horch E., 2018, *AJ*, 155, 27. doi:10.3847/1538-3881/aa9f0e
- Collier Cameron, A. (2016) "Chapter 2: Extrasolar Planetary Transits" in Bozza, V. et al. (ed.) *Methods of Detecting Exoplanets: 1st Advanced School on Exoplanetary Science*.
- Collier Cameron A., Mortier A., Phillips D., Dumusque X., Haywood R. D., Langelier N., Watson C. A., et al., 2019, *MNRAS*, 487, 1082. doi:10.1093/mnras/stz1215 Springer International Publishing AG, pp. 89-131
- Delrez L., Madhusudhan N., Lendl M., Gillon M., Anderson D. R., Neveu-VanMalle M., Bouchy F., et al., 2018, *MNRAS*, 474, 2334. doi:10.1093/mnras/stx2896
- Evans D. F., Southworth J., Smalley B., 2016, *ApJL*, 833, L19. doi:10.3847/2041-8213/833/2/L19
- Faedi F., Gómez Maqueo Chew Y., Pollacco D., Brown D. J. A., Hébrard G., Maltby B., Lam K. W. F., et al., 2016, arXiv, arXiv:1608.04225
- Fouesneau M., 2022, pyphot, doi://10.5281/zenodo.7016775
- Gaia Collaboration, Vallenari A., Brown A. G. A., Prusti T., de Bruijne J. H. J., Arenou F., Babusiaux C., et al., 2023, *A&A*, 674, A1. doi:10.1051/0004-6361/202243940
- Gaia Collaboration, Brown A. G. A., Vallenari A., Prusti T., de Bruijne J. H. J., Babusiaux C., Biermann M., et al., 2021, *A&A*, 649, A1. doi:10.1051/0004-6361/202039657
- Gillon M., Anderson D. R., Collier-Cameron A., Delrez L., Hellier C., Jehin E., Lendl M., et al., 2014, *A&A*, 562, L3. doi:10.1051/0004-6361/201323014
- Ginsburg A., Sipőcz B., Parikh M., Brasseur C. E., Jcsegovia, Groener A., Norman H., et al., 2021, *astropy/astroquery*, doi://10.5281/zenodo.5804082
- Goswamy T., Collier Cameron A., Wilson, T. G., 2024, Dataset, University of St Andrews Research Portal, <https://doi.org/10.17630/1ceff0e3-c2aa-40d0-996a-0d3f8d81cf19>
- Goswamy T., Collier Cameron A., Wilson, T. G., 2024, Software, University of St Andrews Research Portal, <https://doi.org/10.17630/72a692c8-dd85-4078-99d3-8a5551727ff9>
- Hatzes, A. P. (2016) "Chapter 1: The Radial Velocity Method for the Detection of Exoplanets" in Bozza, V. et al. (ed.) *Methods of Detecting Exoplanets: 1st Advanced School on Exoplanetary Science*. Springer International Publishing AG, pp. 3-86.
- Hellier C., Anderson D. R., Bouchy F., Burdanov A., Collier Cameron A., Delrez L., Gillon M., et al., 2019, *MNRAS*, 482, 1379. doi:10.1093/mnras/sty2741
- Horch E. P., Veillette D. R., Baena Gallé R., Shah S. C., O'Rielly G. V., van Altena W. F., 2009, *AJ*, 137, 5057. doi:10.1088/0004-6256/137/6/5057
- Marcussen M. L., Albrecht S. H., 2023, *AJ*, 165, 266. doi:10.3847/1538-3881/acd53d
- Matson R. A., Howell S. B., Ciardi D. R., 2019, *AJ*, 157, 211. doi:10.3847/1538-3881/ab1755
- Maxted P. F. L., Anderson D. R., Collier Cameron A., Delrez L., Gillon M., Hellier C., Jehin E., et al., 2016, *A&A*, 591, A55. doi:10.1051/0004-6361/201628250
- Mayor M., Pepe F., Queloz D., Bouchy F., Rupprecht G., Lo Curto G., Avila G., et al., 2003, *Msngr*, 114, 20
- Nielsen L. D., Bouchy F., Turner O. D., Anderson D. R., Barkaoui K., Benkhaldoun Z., Burdanov A., et al., 2019, *MNRAS*, 489, 2478. doi:10.1093/mnras/stz2351
- Ochsenbein F., Bauer P., Marcout J., 2000, *A&AS*, 143, 23. doi:10.1051/aas:2000169
- Payne A. N., Ciardi D. R., Kane S. R., Carter B., 2018, *AJ*, 156, 209. doi:10.3847/1538-3881/aae310
- Penoyre Z., Belokurov V., Evans N. W., 2022, *MNRAS*, 513, 2437. doi:10.1093/mnras/stac959
- Perruchot S., Kohler D., Bouchy F., Richaud Y., Richaud P., Moreaux G., Merzougui M., et al., 2008, *SPIE*, 7014, 70140J. doi:10.1117/12.787379
- Pollacco D. L., Skillen I., Collier Cameron A., Christian D. J., Hellier C., Irwin J., Lister T. A., et al., 2006, *PASP*, 118, 1407. doi:10.1086/508556
- Queloz D., Mayor M., Weber L., Blécha A., Burnet M., Confino B., Naef D., et al., 2000, *A&A*, 354, 99
- Schanche N., Hébrard G., Collier Cameron A., Dalal S., Smalley B., Wilson T. G., Boisse I., et al., 2020, *MNRAS*, 499, 428. doi:10.1093/mnras/staa2848
- Silva Aguirre V., Davies G. R., Basu S., Christensen-Dalsgaard J., Creevey O., Metcalfe T. S., Bedding T. R., et al., 2015, *MNRAS*, 452, 2127. doi:10.1093/mnras/stv1388
- Silva Aguirre V., Lund M. N., Antia H. M., Ball W. H., Basu S., Christensen-Dalsgaard J., Lebreton Y., et al., 2017, *ApJ*, 835, 173. doi:10.3847/1538-4357/835/2/173
- Skrutskie M. F., Cutri R. M., Stiening R., Weinberg M. D., Schneider S., Carpenter J. M., Beichman C., et al., 2006, *AJ*, 131, 1163. doi:10.1086/498708
- Southworth J., 2010, *MNRAS*, 408, 1689. doi:10.1111/j.1365-2966.2010.17231.x
- Southworth J., 2011, *MNRAS*, 417, 2166. doi:10.1111/j.1365-2966.2011.19399.x
- Southworth J., Bohn A. J., Kenworthy M. A., Ginski C., Mancini L., 2020, *A&A*, 635, A74. doi:10.1051/0004-6361/201937334
- Southworth J., Faedi F., 2022, *Obs*, 142, 1
- Stevens D. J., Collins K. A., Gaudi B. S., Beatty T. G., Siverd R. J., Bieryla A., Fulton B. J., et al., 2017, *AJ*, 153, 178. doi:10.3847/1538-3881/aa5ffb
- STScI Development Team, 2013, *ascl.soft.1303.023*
- Winn J. N., 2009, *IAUS*, 253, 99. doi:10.1017/S174392130802629X
- Wöllert M., Brandner W., 2015, *A&A*, 579, A129. doi:10.1051/0004-6361/201526525
- Wright E. L., Eisenhardt P. R. M., Mainzer A. K., Ressler M. E., Cutri R. M., Jarrett T., Kirkpatrick J. D., et al., 2010, *AJ*, 140, 1868. doi:10.1088/0004-6256/140/6/1868
- Ziegler C., Tokovinin A., Briceño C., Mang J., Law N., Mann A. W., 2020, *AJ*, 159, 19. doi:10.3847/1538-3881/ab55e9

APPENDIX A:

Table A1: R_IRFM and R_trans values along with their errors, used in Fig. 1

WASP host star	R from IRFM	Published R_trans
WASP-001	1.506 ± 0.015	1.470 ± 0.027
WASP-002	0.884 ± 0.013	0.821 ± 0.014
WASP-003	1.339 ± 0.011	1.298 ± 0.049
WASP-004	0.912 ± 0.007	0.910 ± 0.018
WASP-005	1.106 ± 0.008	1.088 ± 0.040
WASP-006	0.817 ± 0.006	0.864 ± 0.025
WASP-007	1.457 ± 0.009	1.478 ± 0.088
WASP-008	0.994 ± 0.012	0.976 ± 0.021
WASP-010	0.736 ± 0.011	0.678 ± 0.030
WASP-011	0.858 ± 0.013	0.772 ± 0.015
WASP-012	1.706 ± 0.025	1.657 ± 0.045
WASP-013	1.544 ± 0.008	1.657 ± 0.079
WASP-014	1.300 ± 0.011	1.318 ± 0.084
WASP-015	1.420 ± 0.011	1.522 ± 0.044
WASP-016	1.084 ± 0.008	1.087 ± 0.042
WASP-017	1.579 ± 0.019	1.583 ± 0.041
WASP-018	1.244 ± 0.007	1.255 ± 0.028
WASP-019	1.003 ± 0.007	1.018 ± 0.015
WASP-020	1.953 ± 0.223	1.242 ± 0.045
WASP-021	1.178 ± 0.009	1.136 ± 0.051
WASP-022	1.212 ± 0.017	1.255 ± 0.030
WASP-023	0.824 ± 0.007	0.819 ± 0.031
WASP-024	1.376 ± 0.013	1.317 ± 0.041
WASP-025	0.916 ± 0.006	0.924 ± 0.018
WASP-026	1.303 ± 0.011	1.284 ± 0.036
WASP-028	1.107 ± 0.008	1.083 ± 0.025
WASP-029	0.787 ± 0.011	0.808 ± 0.044
WASP-030	1.440 ± 0.013	1.389 ± 0.029
WASP-031	1.280 ± 0.012	1.252 ± 0.033
WASP-032	1.155 ± 0.013	1.110 ± 0.050
WASP-033	1.548 ± 0.016	1.509 ± 0.025
WASP-034	1.057 ± 0.005	0.930 ± 0.120
WASP-035	1.119 ± 0.008	1.090 ± 0.030
WASP-036	0.943 ± 0.008	0.985 ± 0.014
WASP-037	1.043 ± 0.012	1.003 ± 0.053
WASP-038	1.495 ± 0.015	1.331 ± 0.028
WASP-039	0.925 ± 0.006	0.939 ± 0.022
WASP-041	0.892 ± 0.005	0.886 ± 0.012
WASP-042	0.862 ± 0.006	0.892 ± 0.021
WASP-043	0.678 ± 0.018	0.667 ± 0.011
WASP-044	0.936 ± 0.012	0.865 ± 0.038
WASP-045	0.908 ± 0.012	0.917 ± 0.024
WASP-046	0.908 ± 0.008	0.858 ± 0.027
WASP-047b	1.151 ± 0.010	1.137 ± 0.013
WASP-047c	1.150 ± 0.010	1.137 ± 0.013
WASP-047d	1.151 ± 0.011	1.137 ± 0.013
WASP-048	1.757 ± 0.014	1.519 ± 0.051
WASP-049	1.024 ± 0.011	1.038 ± 0.037
WASP-050	0.876 ± 0.005	0.855 ± 0.019
WASP-052	0.841 ± 0.008	0.786 ± 0.016
WASP-053	0.837 ± 0.006	0.798 ± 0.023
WASP-054	1.699 ± 0.012	1.828 ± 0.086
WASP-055	1.087 ± 0.009	1.102 ± 0.019
WASP-056	1.199 ± 0.010	1.112 ± 0.024
WASP-057	1.079 ± 0.009	0.927 ± 0.033
WASP-058	1.172 ± 0.011	1.170 ± 0.130

Table A1 continued from previous page

WASP host star	R from IRFM	Published R_trans
WASP-059	0.710 ± 0.015	0.613 ± 0.044
WASP-060	1.488 ± 0.015	1.401 ± 0.066
WASP-061	1.356 ± 0.010	1.390 ± 0.030
WASP-062	1.238 ± 0.008	1.280 ± 0.050
WASP-063	1.755 ± 0.013	1.880 ± 0.080
WASP-064	1.072 ± 0.011	1.058 ± 0.025
WASP-065	1.101 ± 0.009	1.010 ± 0.050
WASP-066	1.785 ± 0.037	1.750 ± 0.090
WASP-067	0.867 ± 0.006	0.817 ± 0.022
WASP-068	1.684 ± 0.011	1.690 ± 0.085
WASP-069	0.847 ± 0.019	0.813 ± 0.028
WASP-070	1.250 ± 0.019	1.251 ± 0.079
WASP-071	2.144 ± 0.021	2.260 ± 0.170
WASP-072	2.180 ± 0.030	1.980 ± 0.240
WASP-073	2.213 ± 0.017	2.070 ± 0.135
WASP-074	1.531 ± 0.008	1.536 ± 0.026
WASP-075	1.306 ± 0.012	1.270 ± 0.020
WASP-076	1.836 ± 0.037	1.765 ± 0.071
WASP-077	1.071 ± 0.028	0.955 ± 0.015
WASP-078	2.031 ± 0.023	2.350 ± 0.095
WASP-079	1.590 ± 0.010	1.510 ± 0.035
WASP-080	0.650 ± 0.015	0.593 ± 0.012
WASP-081	1.241 ± 0.013	1.283 ± 0.039
WASP-082	2.086 ± 0.015	2.219 ± 0.087
WASP-083	1.057 ± 0.010	1.050 ± 0.050
WASP-084	0.817 ± 0.006	0.768 ± 0.019
WASP-085	1.157 ± 0.043	0.935 ± 0.023
WASP-086	2.136 ± 0.016	1.291 ± 0.014
WASP-087	1.623 ± 0.019	1.627 ± 0.062
WASP-088	2.131 ± 0.029	2.080 ± 0.090
WASP-089	0.904 ± 0.010	0.880 ± 0.030
WASP-090	1.892 ± 0.031	1.980 ± 0.090
WASP-091	0.856 ± 0.007	0.860 ± 0.030
WASP-092	1.286 ± 0.016	1.341 ± 0.058
WASP-093	1.629 ± 0.019	1.524 ± 0.040
WASP-094	1.567 ± 0.012	1.620 ± 0.045
WASP-095	1.213 ± 0.010	1.130 ± 0.060
WASP-096	1.081 ± 0.010	1.050 ± 0.050
WASP-097	1.090 ± 0.008	1.060 ± 0.040
WASP-098	0.735 ± 0.006	0.741 ± 0.021
WASP-099	1.688 ± 0.013	1.760 ± 0.085
WASP-100	1.723 ± 0.014	1.670 ± 0.145
WASP-101	1.311 ± 0.009	1.290 ± 0.040
WASP-102	1.389 ± 0.016	1.331 ± 0.013
WASP-103	1.757 ± 0.100	1.413 ± 0.045
WASP-104	0.935 ± 0.006	0.935 ± 0.010
WASP-105	1.093 ± 0.028	0.900 ± 0.030
WASP-106	1.481 ± 0.013	1.393 ± 0.038
WASP-107	0.661 ± 0.014	0.670 ± 0.020
WASP-108	1.247 ± 0.016	1.215 ± 0.040
WASP-109	1.412 ± 0.019	1.346 ± 0.044
WASP-110	0.876 ± 0.007	0.881 ± 0.035
WASP-111	1.887 ± 0.015	1.850 ± 0.100
WASP-112	1.082 ± 0.012	1.002 ± 0.037
WASP-113	1.741 ± 0.015	1.608 ± 0.105
WASP-114	1.414 ± 0.017	1.430 ± 0.060
WASP-117	1.213 ± 0.007	1.170 ± 0.063
WASP-118	1.858 ± 0.021	1.754 ± 0.016
WASP-119	1.107 ± 0.009	1.200 ± 0.100
WASP-120	1.707 ± 0.015	1.870 ± 0.110

Table A1 continued from previous page

WASP host star	R from IRFM	Published R_trans
WASP-121	1.473 ± 0.008	1.440 ± 0.030
WASP-122	1.454 ± 0.010	1.520 ± 0.030
WASP-123	1.221 ± 0.017	1.285 ± 0.051
WASP-124	1.147 ± 0.010	1.020 ± 0.020
WASP-126	1.192 ± 0.013	1.270 ± 0.075
WASP-127	1.354 ± 0.012	1.333 ± 0.027
WASP-128	1.203 ± 0.010	1.152 ± 0.019
WASP-129	1.185 ± 0.012	0.900 ± 0.020
WASP-130	1.035 ± 0.008	0.960 ± 0.030
WASP-131	1.673 ± 0.021	1.526 ± 0.065
WASP-132	0.740 ± 0.010	0.740 ± 0.020
WASP-133	1.507 ± 0.017	1.440 ± 0.050
WASP-134	1.165 ± 0.010	1.175 ± 0.048
WASP-135	0.889 ± 0.008	0.960 ± 0.050
WASP-136	2.071 ± 0.019	2.210 ± 0.220
WASP-137	1.634 ± 0.014	1.520 ± 0.110
WASP-138	1.448 ± 0.013	1.360 ± 0.050
WASP-139	0.818 ± 0.007	0.800 ± 0.040
WASP-140	0.817 ± 0.011	0.870 ± 0.040
WASP-141	1.316 ± 0.013	1.370 ± 0.070
WASP-142	1.642 ± 0.022	1.640 ± 0.080
WASP-143	0.992 ± 0.010	1.013 ± 0.032
WASP-144	1.108 ± 0.032	0.810 ± 0.040
WASP-145	0.674 ± 0.010	0.680 ± 0.070
WASP-146	1.314 ± 0.020	1.232 ± 0.072
WASP-147	1.441 ± 0.016	1.370 ± 0.080
WASP-148	0.926 ± 0.008	1.030 ± 0.200
WASP-150	1.710 ± 0.024	1.651 ± 0.027
WASP-151	1.220 ± 0.011	1.181 ± 0.020
WASP-153	1.654 ± 0.020	1.730 ± 0.095
WASP-156	0.824 ± 0.005	0.760 ± 0.030
WASP-157	1.091 ± 0.014	1.134 ± 0.051
WASP-158	1.571 ± 0.025	1.390 ± 0.180
WASP-159	2.065 ± 0.022	2.110 ± 0.100
WASP-160	0.847 ± 0.008	0.872 ± 0.030
WASP-161	1.612 ± 0.278	1.712 ± 0.078
WASP-162	1.168 ± 0.010	1.110 ± 0.050
WASP-163	1.194 ± 0.014	1.015 ± 0.039
WASP-164	0.957 ± 0.012	0.932 ± 0.029
WASP-165	1.699 ± 0.028	1.650 ± 0.090
WASP-166	1.240 ± 0.010	1.220 ± 0.060
WASP-167	1.916 ± 0.028	1.790 ± 0.050
WASP-168	1.087 ± 0.007	1.120 ± 0.060
WASP-169	2.247 ± 0.028	2.011 ± 0.139
WASP-170	1.016 ± 0.017	0.938 ± 0.059
WASP-171	1.989 ± 0.022	1.637 ± 0.069
WASP-172	2.101 ± 0.031	1.910 ± 0.100
WASP-173	1.069 ± 0.010	1.110 ± 0.050
WASP-174	1.381 ± 0.014	1.347 ± 0.018
WASP-175	1.244 ± 0.012	1.204 ± 0.064
WASP-176	2.005 ± 0.022	1.925 ± 0.046
WASP-177	0.802 ± 0.008	0.885 ± 0.046
WASP-178	1.700 ± 0.018	1.670 ± 0.070
WASP-180	1.177 ± 0.012	1.190 ± 0.060
WASP-181	1.017 ± 0.010	0.965 ± 0.043
WASP-182	1.241 ± 0.011	1.340 ± 0.030
WASP-183	0.873 ± 0.008	0.871 ± 0.038
WASP-184	1.761 ± 0.020	1.650 ± 0.090
WASP-185	1.586 ± 0.015	1.500 ± 0.080
WASP-189	2.343 ± 0.028	2.360 ± 0.030

Table A1 continued from previous page

WASP host star	R from IRFM	Published R_trans
WASP-190	1.811 ± 0.028	1.600 ± 0.100
WASP-192	1.317 ± 0.015	1.320 ± 0.070

This paper has been typeset from a \TeX/L\AA\TeX file prepared by the author.